International Journal of Minerals, Metallurgy and Materials
Volume 24, Number 4, April 2017, Page 455
DOI: 10.1007/s12613-017-1426-1

One-pot synthesis and optical properties of In- and Sn-doped ZnO nanoparticles

Li-ping Wang, Fu Zhang, Shuai Chen, and Zi-heng Bai

Department of Materials Physics and Chemistry, School of Materials Science and Engineering, University of Science and Technology Beijing, Beijing 100083, China
(Received: 13 October 2016; revised: 1 November 2016; accepted: 7 November 2016)

Abstract: Colloidal indium-doped zinc oxide (IZO) and tin-doped zinc oxide (ZTO) nanoparticles were successfully prepared in organic solution, with metal acetylacetonate as the precursor and oleylamine as the solvent. The crystal and optical properties were characterized by X-ray diffraction, UV−visible spectrophotometry, and fluorescence spectroscopy, respectively; the surface and structure morphologies were observed by scanning electron microscopy and transmission electron microscopy. The XRD patterns of the IZO and ZTO nanoparticles all exhibited similar diffraction peaks consistent with the standard XRD pattern of ZnO, although the diffraction peaks of the IZO and ZTO nanoparticles were slightly shifted with increasing dopant concentration. With increasing dopant concentration, the fluorescent emission peaks of the IZO nanoparticles exhibited an obvious red shift because of the difference in atomic radii of indium and zinc, whereas those of the ZTO nanoparticles exhibited almost no shift because of the similarity in atomic radii of tin and zinc. Furthermore, the sizes of the IZO and ZTO nanoparticles distributed in the ranges 20–40 and 20–25 nm, respectively, which is attributed to the difference in ionic radii of indium and tin.

Keywords: nanoparticles; zinc oxide; indium; tin; doping; synthesis; optical properties

1. Introduction

Semiconductor materials have attracted much research interest because of their broad range of applications in various fields in modern information society. Metal oxides, with a band gap of 2–3 eV or greater, usually have a low carrier concentration and high resistivity at room temperature [1]. When incorporated into a donor or acceptor impurity, the metal oxides can become semiconductors. If their band gap is greater than 3.1 eV, metal oxide semiconductors will exhibit excellent transparent performance in the visible region and exhibit an electrical conductivity comparable to that of metals [2–3]. In the case of In_2O_3, for instance, the resistivity of an Sn-doped In_2O_3 (ITO) thin film can be as low as 7.5×10^{-5} Ω·cm and its average light transmittance in the visible region can be as high as 90% [4]. Metal oxide semiconductors therefore have a wide range of applications in solar cells [5–6], light-emitting diodes [7], field-effect transistors [8–12], and other devices [13–14]. Current research on metal oxide semiconductors is mainly focused on In_2O_3, ZnO, SnO_2, Ga_2O_3, and their metal alloys.

Wurtzite-structured ZnO is a semiconductor with a wide direct band gap, E_g = 3.37 eV; it exhibits excellent optical, electrical, magnetic, piezoelectric, thermoelectric, ferroelectric, and gas- and pressure-sensitive performances [15–17]. Extensive research efforts have been devoted to ZnO for decades. With the advancement of such research, ZnO has gradually attracted more interest as a new superior short-wave-emitting material whose range of applications is constantly expanding. When ZnO is doped with suitable donors, its resistivity is effectively reduced and its conductivity correspondingly improved [18]. Because ZnO itself is a polar semiconductor that exhibits n-type conductivity with an electron concentration in the range from 10^{17} to 10^{18} cm^{-3}, n-type doped ZnO nanomaterials are easily obtained through doping with appropriate metal ions. The elements suitable for n-type doping are mainly those of groups III and IV, such as Al, In, Ga, and Sn. For instance, Rozati *et al.* [19] used a pyrolysis technique to synthesize indium-doped zinc oxide (IZO) and investigated the effect of substrate temperature on

Corresponding author: Li-ping Wang E-mail: lpwang@mater.ustb.edu.cn

its physical properties. Fu *et al.* [20] reported the synthesis of Zn_2SnO_4, a certain kind of tin-doped zinc oxide (ZTO), using a hydrothermal method in a water/ethylene glycol solution containing amines (ethylamine, *n*-butylamine, *n*-hexylamine, and *n*-octylamine) as mineralizers. Shi *et al.* [21] synthesized IZO nanowires using electrodeposition and oxidation methods and subsequently characterized them by atomic force microscopy (AFM) and measurements of their optical properties. Thus, these previous studies indicate that the morphology and properties of IZO and ZTO vary depending on the synthetic route.

Various methods have been developed to prepare undoped and doped ZnO; however, many of these methods have shortcomings, such as a broad size distribution, low crystallinity, high cost, and complex operation, etc. Recently, Choi *et al.* [22] reported a simple one-pot synthesis of colloidal, monodispersed, and highly crystalline ITO nanoparticles.

In this work, we synthesized IZO and ZTO nanoparticles in one pot under an N_2 environment using metal acetylacetonate and oleylamine as the precursor and reaction solvent, respectively. The dopant concentration was varied in the range from 3at% to 10at% to obtain the metal oxide semiconductor. We subsequently investigated the crystallization performance, size distribution, and optical properties of the synthesized IZO and ZTO nanoparticles using X-ray diffraction (XRD), scanning electron microscopy (SEM), transmission electron microscopy (TEM), UV–visible (UV–vis) spectrophotometry, and photoluminescence (PL) spectroscopy.

2. Experimental

2.1. Materials

Zinc acetylacetonate ($Zn(acac)_2$, purity > 96.0%), tin bis(acetylacetonate) dichloride ($Sn(acac)_2Cl_2$, purity 98%), and oleylamine ($C_{18}H_{37}N$, purity > 50%) were purchased from Tokyo Chemical Industry (TCI). Indium acetylacetonate ($In(acac)_3$, purity > 99.9%) was purchased from Sigma-Aldrich. All chemicals were used as received without further purification.

2.2. Synthesis of IZO and ZTO nanoparticles

A typical preparation of IZO nanoparticles was carried out as follows. A slurry of $In(acac)_3$ and $Zn(acac)_2$ metal precursors was first added to a 50-mL three-neck flask in an appropriate molar ratio, such as In/Zn = 3%, 5%, and 10%. Oleylamine was then added to ensure a $(Zn^{2+} + In^{3+})$/oleylamine molar ratio of 1:48. The reaction system was pumped with a diaphragm vacuum pump and filled with nitrogen. The procedure was repeated three times to ensure that the reaction system was completely kept in a nitrogen atmosphere. After that, the reaction mixture was heated at 210°C for 5 h under continuous stirring. After the reaction was completed, the system was gradually cooled to room temperature and an excess amount of ethanol was added to the solution to induce precipitation of nanoparticles. The precipitate was centrifuged and washed with ethanol three times. The obtained product was divided into two parts: one was dried in a vacuum oven for SEM and XRD characterization, and the other was dispersed in dichloromethane for collected of the UV–vis absorption and PL spectra and for TEM observation.

The method used to prepare ZTO nanoparticles was similar to that used to prepare the IZO nanoparticles, except with $Sn(acac)_2Cl_2$ and $Zn(acac)_2$ as precursors. The reaction conditions and subsequent processing were the same as those in the synthesis of IZO nanoparticles. During the reaction, oleylamine can accelerate the rate of formation of solid solution while simultaneously serving as a good surfactant. The use of oleylamine can therefore promote the formation of spherical nanoparticles [23].

2.3. Characterization

The crystallinity of the IZO and ZTO nanoparticles was characterized using a DMAX-RB X-ray diffractometer equipped with a Cu K_α radiation source operated at 40 kV and 150 mA; the instrument was operated in reflection mode and at a scanning rate of $10°\cdot min^{-1}$. The UV–vis absorption spectra and fluorescence emission spectra were collected on a JASCO V570 spectrophotometer and FL-4500 spectrophotometer, respectively. The morphology of the IZO and ZTO nanoparticles was observed using a FEI-F20 transmission electron microscope and an S-4800 scanning electron microscope.

3. Results and discussion

3.1. Optical properties

UV–vis absorption spectra of IZO and ZTO nanoparticles with various doping concentrations of In and Sn ions are shown in Figs. 1 and 2, respectively. A maximum absorption peak is observed at approximately 232 nm and a low absorption peak with similar strength is observed at approximately 275 nm for both IZO and ZTO nanoparticles. The difference is that the maximum absorption peak for IZO exhibits a slight red shift with increasing dopant concentration: it shifts to 231, 234, and 239 nm for samples with a

doping concentration of 3%, 5%, and 10%, respectively. On the contrary, no obvious red or blue shifts are observed for the absorption peaks of the ZTO nanoparticles.

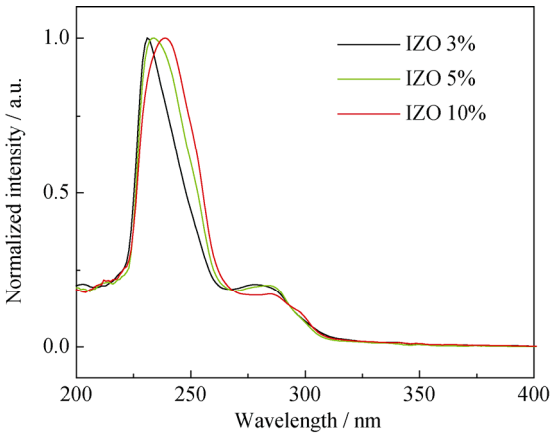

Fig. 1. UV–vis absorption spectra of the IZO nanoparticles with 3%, 5%, and 10% of In ions.

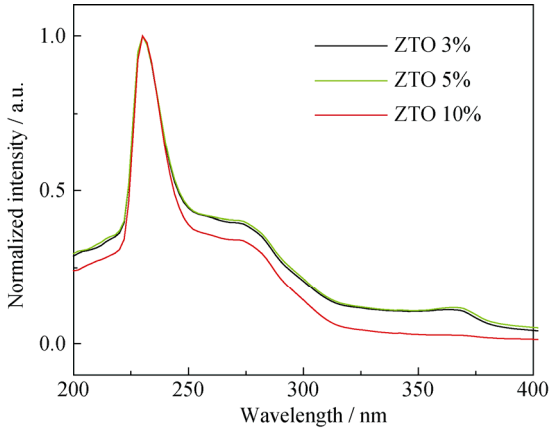

Fig. 2. UV–vis absorption spectra of the ZTO nanoparticles with 3%, 5%, and 10% of Sn ions.

The difference in the UV–vis absorption features for IZO and ZTO are ascribed to the radius difference between indium and tin ions. The reason for the red shift with increasing doping concentration of indium in IZO may be due to the replacement of Zn^{2+} ions (0.074 nm) by In^{3+} ions with a larger ionic radius (0.081 nm) in the IZO crystals. The defect energy level is well known to lie between the valence band and the conduction band. When a crystal is doped, the electrons and holes will recombine between the defect level and the valence band of the impurity, causing a shift of the absorption or emission peak [24]. With increasing In^{3+} concentration, the concentration of defects in the crystal increases and the band gap decreases. However, with increasing In^{3+} concentration, the average size of IZO nanoparticles may increase, leading to diminished quantum effects. Therefore, the maximum absorption peak of IZO exhibits a red shift. In the case of the ZTO nanoparticles, the ionic radius of Sn^{4+} (0.071 nm) is similar to that of Zn^{2+} (0.074 nm); as a result, no obvious shift is observed with different concentrations of tin ions.

PL spectra of the IZO nanoparticles with various concentrations of indium ions are shown in Fig. 3. Two obvious emission peaks appear at approximately 410 and 470 nm. With increasing indium content, the main peak exhibits an obvious red shift. However, the second peak shows no obvious deviation and its relative intensity increases substantially. According to the literature, the main emission peak generally corresponds to an exciton emission peak, whereas the second peak is caused by defects or dopants in a sample [25]. The results of this previous work suggest that the defects in IZO increase with increasing indium content. Table 1 shows the maximum emission peak and the band-gap value calculated from the emission spectra of IZO. These results indicate that the band gap decreases with increasing doping concentration of In ions.

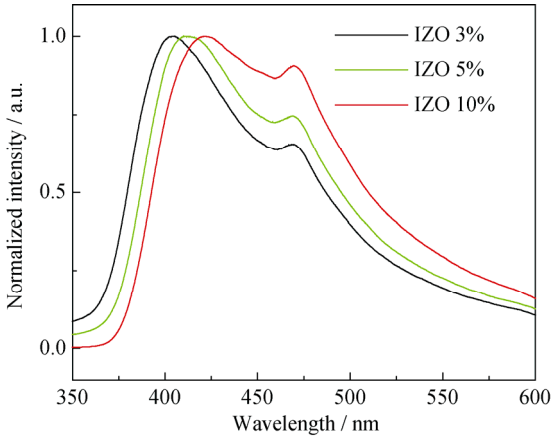

Fig. 3. Fluorescence emission spectra of the IZO nanoparticles with 3%, 5%, and 10% of In; the excitation wavelength is 275 nm.

Table 1. Band gap values of the IZO nanoparticles calculated from the fluorescence emission spectra with an excitation wavelength of 275 nm

In^{3+} content / %	Emission peak / nm	Calculated band gap / eV
3	404	3.07
5	413	3.01
10	422	2.94

Fig. 4 shows the PL emission spectra of the ZTO nanoparticles. No significant shift is observed for any emission peak, and the results of the fluorescence emission characterization are consistent with those of the UV–vis absorption characterization. The fluorescent emission peak of the ZTO appears at 345 nm, and the band gap of ZTO is 3.60 eV,

which is higher than that of ZnO (3.37 eV). By contrast, the fluorescent emission peak of the IZO appears at 410 nm and the band gap of IZO is approximately 3.03 eV, which is lower than that of ZnO. These difference fluorescent emission characteristics are also caused by the different ionic radii of the doping elements.

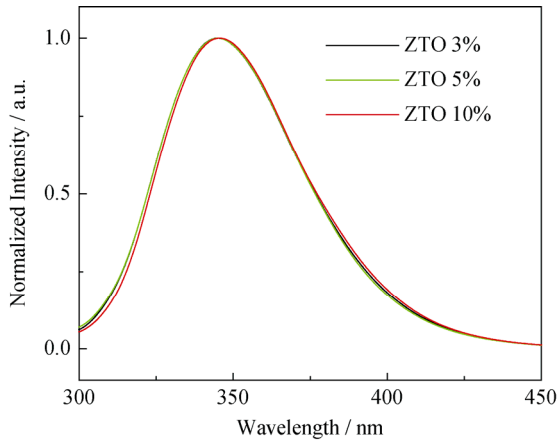

Fig. 4. Fluorescence emission spectra of the ZTO nanoparticles with 3%, 5%, and 10% of Sn; the excitation wavelength is 275 nm.

Notably, the UV–vis absorption and PL spectra change only slightly for the IZO nanoparticles and even remain constant for the ZTO nanoparticles at various doping concentrations, which may be detrimental for certain applications that require a relatively high emission intensity. However, it is advantageous for applications that require a medium emission intensity in visible-light region. In addition, if elements with ionic radii greater than the ionic radius of In^{3+} are used as dopants, the doped nanoparticles might exhibit substantially different emission characteristics compared to those of IZO.

3.2. Crystal properties

The XRD patterns of the IZO nanoparticles are shown in Fig. 5; the indexing of the major crystal planes—(100), (002), and (101)—is shown in Fig. 6 for the 2θ range from 30° to 40°. All diffraction peaks of the IZO nanoparticles match well with those of the standard wurtzite ZnO (JCPDS No. 36-1451) [26], except that a slight deviation from the corresponding peak position for ZnO is observed for each diffraction peak. This deviation is attributed to the replacement of In^{3+} with Zn^{2+} with different ionic radii and demonstrates that, when the doping concentration is low, the crystal structure does not obviously change; it also demonstrates that sharp, high-intensity diffraction peaks indicate good crystalline properties of the IZO nanoparticles. According to the Debye–Scherrer equation, the calculated average crystallite size of IZO is 17.8, 18.3, and 18.1 nm for the IZO nanoparticles with indium contents of 3%, 5%, and 10%, respectively.

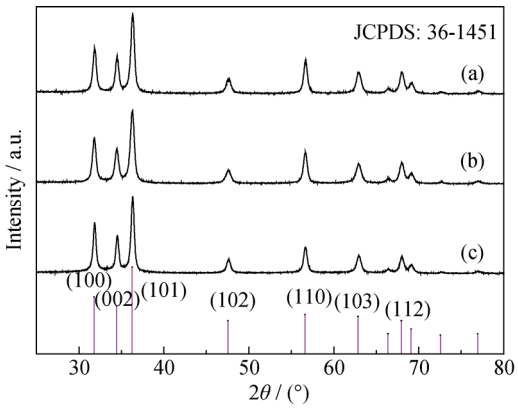

Fig. 5. XRD patterns of the IZO nanoparticles doped with 3% (a), 5% (b), and 10% of In^{3+} (c).

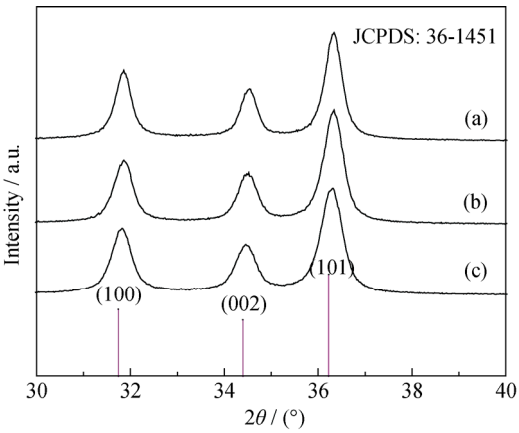

Fig. 6. XRD patterns in the 2θ range from 30 to 40° for the IZO nanoparticles doped with 3% (a), 5% (b), and 10% of In^{3+} (c).

The XRD patterns of the ZTO nanoparticles with different tin contents are shown in Fig. 7. All of the patterns show strong diffraction peaks corresponding to the (100), (002), and (101) planes. When the relative intensity of the (101) plane (I_1) was set to 100%, the relative intensities of the (100) (I_2) and (002) (I_3) planes were calculated to be 55.1% and 41.1%, respectively. Meanwhile, each diffraction peak is consistent with the standard line of wurtzite ZnO, indicating that the crystallization behavior of ZnO doped with a small amount of tin is the same as that of ZnO. This result suggests that no SnO_2 or Zn_2SnO_4 is generated separately in the reaction. During the synthesis, Sn^{4+} replaces Zn^{2+} in the ZnO lattice and generates a solid solution of zinc and tin oxides. The average crystallite size of ZTO calculated according to the Debye–Scherrer equation is 13.9, 15.1, and 16.5 nm for the nanoparticles with tin contents of 3%, 5% and 10%, respectively.

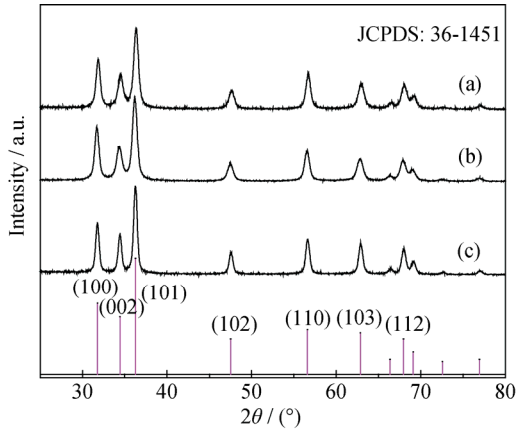

Fig. 7. XRD patterns of ZTO doped with 3% (a), 5% (b), and 10% (c) of Sn^{4+}.

3.3. Surface and structure morphology

Fig. 8 shows the SEM images of the IZO and ZTO nanoparticles. The IZO and ZTO nanoparticles distribute uniformly and compactly with good surface morphology, and most are spherical except for a small number with polygonal shapes. These polygonal particles may be due to the agglomeration of nanoparticles doped with In and Sn. In addition, the ZTO nanoparticle size distributes between 20 and 25 nm, whereas the IZO nanoparticles are larger, ranging from 20 to 40 nm. Compared with the XRD analysis results, the nanoparticle sizes observed in the SEM images are much larger. One possible reason for this discrepancy is that the size calculated by the Debye–Scherrer equation is that of crystallites and is an approximation [27]. Another possible reason is that spherical particles are polycrystalline, containing more than one IZO or ZTO crystallite.

The TEM images of the IZO and ZTO nanoparticles are shown in Fig. 9. The shape and size of the obtained nanoparticles are all consistent with that shown in the SEM images. The ZTO nanoparticles are almost spherical with a more uniform size distribution, whereas the IZO nanoparticles

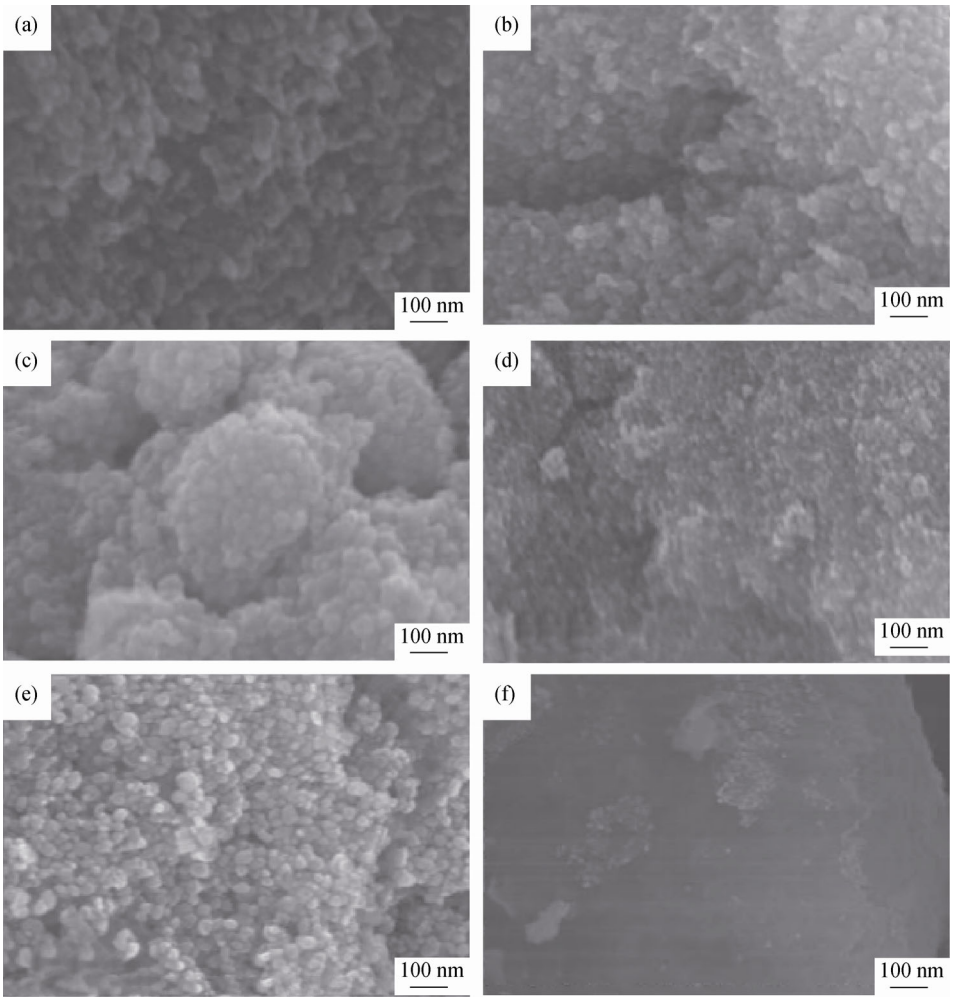

Fig. 8. SEM images of the IZO nanoparticles doped with 3% (a), 5% (b), and 10% (c) of In^{3+} and the ZTO nanoparticles doped with 3% (d), 5% (e), and 10% (f) of Sn^{4+}.

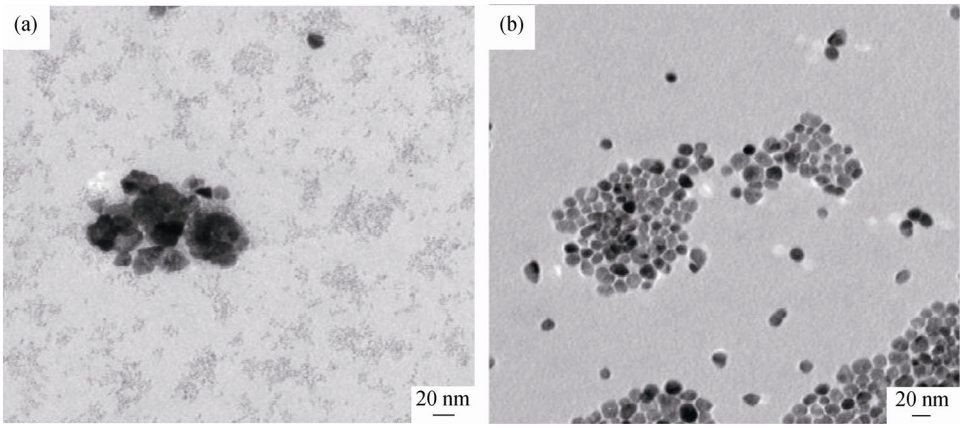

Fig. 9. TEM images of the IZO (a) and ZTO (b) nanoparticles.

are uniform and some are larger and clearly agglomerated. This difference between IZO and ZTO shapes and sizes may be due to the difference in their ionic radii. When Zn^{2+} is substituted by larger In^{3+}, more impurity defects appear within the nanoparticles, ultimately resulting in an irregular particle shape. However, the ionic radii of Sn^{4+} and Zn^{2+} are very similar; the ZTO nanoparticles are therefore more regular in shape and size.

4. Conclusion

IZO and ZTO nanoparticles with colloidal performance and good optical properties were successfully prepared via solution method involving the one-pot thermal decomposition of metal acetylacetonate in an oleylamine solvent. ZnO nanoparticles doped with a small amount of metal ions with an ionic radius similar to that of Zn^{2+} does not change the crystal properties of the ZnO, whereas the XRD diffraction peaks slightly shift because of the difference in ionic radius between Zn^{2+} and the dopant metal ions. In addition, the difference in ionic radius of the doping element also affects the optical properties and the nanoparticle size and morphology. With increasing impurity concentration, the fluorescence emission peaks of IZO exhibit an obvious red shift, whereas those of ZTO exhibit almost no shift. The energy band gap of IZO is higher than that of ZnO, whereas the band gap of ZTO is lower.

Acknowledgement

The authors gratefully acknowledge financial support from the National Natural Science Foundation of China (Grant No. 21073012).

References

[1] E.H. Nicollian and J.R. Brews, *MOS* (*Metal Oxide Semiconductor*) *Physics and Technology*, Wiley, New York, 1982, 15.

[2] S.G. Lim, S. Kriventsov, T.N. Jackson, J.H. Haeni, D.G. Schlom, A.M. Balbashov, R. Uecker, P. Reiche, J.L. Freeouf, and G. Lucovsky, Dielectric functions and optical bandgaps of high-*K* dielectrics for metal-oxide-semiconductor field-effect transistors by far ultraviolet spectroscopic ellipsometry, *J. Appl. Phys.*, 91(2002), No. 7, p. 4500.

[3] E. Monroy, F. Omnès, and F. Calle, Wide-bandgap semiconductor ultraviolet photodetectors, *Semicond. Sci. Technol.*, 18(2003), No. 4, p. R33.

[4] O.N. Mryasov and A.J. Freeman, Electronic band structure of indium tin oxide and criteria for transparent conducting behavior, *Phys. Rev. B*, 64(2001), No. 23, article No. 233111.

[5] R.J. Stirn and Y.C.M. Yeh, Technology of GaAs metal-oxide-semiconductor solar cells, *IEEE Trans. Electron Devices*, 24(1977), No. 4, p. 476.

[6] K. Hara, T. Horiguchi, T. Kinoshita, K. Sayama, H. Sugihara, and H. Arkawa, Highly efficient photon-to-electron conversion with mercurochrome-sensitized nanoporous oxide semiconductor solar cells, *Sol. Energy Mater. Sol. Cells*, 64(2000), No. 2, p. 115.

[7] M. Kulakci, U. Serincan, and R. Turan, Electroluminescence generated by a metal oxide semiconductor light emitting diode (MOS-LED) with Si nanocrystals embedded in SiO_2 layers by ion implantation, *Semicond. Sci. Technol.*, 21(2006), No. 12, p. 1527.

[8] K. Natori, Ballistic metal-oxide-semiconductor field effect transistor, *J. Appl. Phys.*, 76(1994), No. 8, p. 4879.

[9] H.Q. Chiang, J.F. Wager, R.L. Hoffman, J. Jeong, and D.A. Keszler, High mobility transparent thin-film transistors with amorphous zinc tin oxide channel layer, *Appl. Phys. Lett.*, 86(2005), No. 1, article No. 013503.

[10] Y.L. Zhao, G.F. Dong, L. Duan, J. Qiao, D.Q. Zhang, L.D. Wang, and Y. Qiu, Impacts of Sn precursors on solution-processed amorphous zinc–tin oxide films and their transistors, *RSC Adv.*, 2(2012), No. 12, p. 5307.

[11] J. Socratous, K.K. Banger, Y. Vaynzof, A. Sandhanala, A.D. Brown, A. Sepe, U. Steiner, and H. Sirringhaus, Electronic structure of low-temperature solution-processed amorphous metal oxide semiconductors for thin-film transistor applica-

tions, *Adv. Funct. Mater.*, 25(2015), No. 12, p. 1873.

[12] K. Domen, T. Miyase, K. Abe, H. Hosono, and T. Kamiya, Positive gate bias instability induced by diffusion of neutral hydrogen in amorphous In–Ga–Zn–O thin-film transistor, *IEEE Electron Device Lett.*, 35(2014), No. 8, p. 832.

[13] A. Liu, R. Jones, L. Liao, D. Samara-Rubio, D. Rubin, O. Cohen, R. Nicolaescu, and M. Paniccia, A high-speed silicon optical modulator based on a metal-oxide-semiconductor capacitor, *Nature*, 427(2004), No. 6975, p. 615.

[14] C.T. Black, K.W. Guarini, Y. Zhang, H. Kim, J. Benedict, E. Sikorski, I.V. Babich, and K.R. Milkove, High-capacity, self-assembled metal-oxide-semiconductor decoupling capacitors, *IEEE Electron Device Lett.*, 25(2004), No. 9, p. 622.

[15] S. Choi, B.C. Johnson, S. Castelletto, C. Ton-That, M.R. Phillips, and I. Aharonovich, Single photon emission from ZnO nanoparticles, *Appl. Phys. Lett.*, 104(2014), No. 26, article No. 261101.

[16] F. Lu, W.P. Cai, and Y.G. Zhang, ZnO hierarchical micro/nanoarchitectures: solvothermal synthesis and structurally enhanced photocatalytic performance, *Adv. Funct. Mater.*, 18(2008), No. 7, p. 1047.

[17] T.G. Xu, L.W. Zhang, H.Y. Cheng, and Y.F. Zhu, Significantly enhanced photocatalytic performance of ZnO via graphene hybridization and the mechanism study, *Appl. Catal. B*, 101(2011), No. 3-4, p. 382.

[18] R. Deng, Y.F. Li, B. Yao, J.M. Qin, D.Y. Jiang, X. Fang, F. Fang, Z.P. Wei, and L.L. Gao, Shallow donor ionization energy in Sn-doped ZnO nanobelts, *Nanosci. Nanotechnol. Lett.*, 6(2014), No. 10, p. 887.

[19] S.M. Rozati, F. Zarenejad, and N. Memarian, Study on physical properties of indium-doped zinc oxide deposited by spray pyrolysis technique, *Thin Solid Films*, 520(2011), No. 4, p. 1259.

[20] X.L. Fu, X.X. Wang, J.L. Long, Z.X. Ding, T.J. Yan, G.Y. Zhang, Z.Z. Zhang, H.X. Lin, and X.Z. Fu, Hydrothermal synthesis, characterization, and photocatalytic properties of Zn_2SnO_4, *J. Solid State Chem.*, 182(2009), No. 3, p. 517.

[21] J.B. Shi, P.F. Wu, Y.T. Lin, C.T. Kao, C.J. Chen, F.C. Cheng, H.H. Liu, Y.C. Chen, H.S. Lin, and H.W. Lee, Synthesis and optical properties of single-crystalline indium zinc oxide (IZO) nanowires via co-deposition and oxidation methods, *Vacuum*, 115(2015), No. 2, p. 61.

[22] S.I. Choi, K.M. Nam, B.K. Park, W.S. Seo, and J.T. Park, Preparation and optical properties of colloidal, monodisperse, and highly crystalline ITO nanoparticles, *Chem. Mater.*, 20(2008), No. 8, p. 2609.

[23] J.F. Liu, Y.Y. Bei, H.P. Wu, D. Shen, J.Z. Gong, X.G. Li, Y.W. Wang, N.P. Jiang, and J.Z. Jiang, Synthesis of relatively monodisperse ZnO nanocrystals from a precursor zinc 2,4-pentanedionate, *Mater. Lett.*, 61(2007), No. 13, p. 2837.

[24] J.M.D. Coey, M. Venkatesan, and C.B. Fitzgerald, Donor impurity band exchange in dilute ferromagnetic oxides, *Nat. Mater.*, 4(2005), No. 2, p. 173.

[25] T. Koida, S.F. Chichibu, A. Uedono, A. Tsukazaki, M. Kawasaki, T. Sota, Y. Segawa, and H. Koinuma, Correlation between the photoluminescence lifetime and defect density in bulk and epitaxial ZnO, *Appl. Phys. Lett.*, 82(2003), No. 4, p. 532.

[26] D.W. Chu, Y.P. Zeng, and D.L. Jiang, Hydrothermal synthesis and optical properties of Pb^{2+} doped ZnO nanorods, *Mater. Lett.*, 60(2006), No. 21-22, p. 2783.

[27] U. Holzwarth and N. Gibson, The Scherrer equation versus the "Debye–Scherrer equation," *Nat. Nanotechnol.*, 6(2011), No. 9, p. 534.